



Cite this: CrystEngComm, 2016, 18, 6689

## Growth of spherical boron oxynitride nanoparticles with smooth and petalled surfaces during a chemical vapour deposition process†

Andrey M. Kovalskii,<sup>\*a</sup> Andrei T. Matveev,<sup>a</sup> Oleg I. Lebedev,<sup>b</sup> Irina V. Sukhorukova,<sup>a</sup> Konstantin L. Firestein,<sup>a</sup> Alexander E. Steinman,<sup>a</sup> Dmitry V. Shtansky<sup>\*a</sup> and Dmitri Golberg<sup>\*c</sup>

A rich variety of hollow and solid (without internal hollow spaces) spherical boron oxynitride nanoparticles (BNO-NPs) with smooth or petalled surfaces were synthesized during a boron oxide-assisted chemical vapour deposition (BOCVD) process. Diverse BNO-NPs were obtained while utilizing different precursors, gas flow rates and synthesis temperatures in the range of 1200–1430 °C. The BNO-NP morphologies, atomic structures and spatially-resolved chemical compositions were studied by scanning (SEM) and transmission electron microscopy (TEM), X-ray diffraction (XRD), energy-dispersive X-ray, Fourier-transform infrared and confocal Raman spectroscopy. Particle size distributions were measured using dynamic light scattering under visual microscopic control. A growth model of different spherical BNO-NP types based on the detailed analysis of physical-chemical processes at different BOCVD stages was proposed. A new type of spherical BNO-NPs of “hedgehog” morphologies with BN nanowires on their surfaces was first predicted in accordance with the designed model and then experimentally verified.

Received 13th May 2016,  
Accepted 13th July 2016

DOI: 10.1039/c6ce01126h

[www.rsc.org/crystengcomm](http://www.rsc.org/crystengcomm)

### 1. Introduction

Hexagonal boron nitride (h-BN) is a layered material exhibiting superb resistance to oxidation, profound chemical inertness and high thermal stability. Over the last decade, there has been a great interest in h-BN nanostructures because of their high thermal conductivity, excellent lubricating properties, low density ( $2.27 \text{ g cm}^{-3}$ ), and good biocompatibility.<sup>1–6</sup>

All the mentioned properties presume different potential applications of BN nanostructures in lubricants and heat resisting materials, functional and superhydrophobic coatings, advanced ceramics and light metal composites, drug delivery systems, catalysts, and hydrogen accumulators.<sup>5–12</sup>

BN nanostructures of various morphologies (nanotubes, nanowires, nanoribbons, nanofibers, nanospheres, nanocages, nano-polyhedra and nanosheets) can be fabricated

through high temperature syntheses ( $>2000 \text{ }^\circ\text{C}$ ), *i.e.* by plasma-chemical methods, arc discharge, and laser ablation; and lower temperature syntheses ( $<2000 \text{ }^\circ\text{C}$ ), *i.e.* carbothermal reaction, ball milling, and chemical vapour deposition (CVD).<sup>13–19</sup> Nowadays, the high-yield methods for obtaining BN nanotubes are the plasma-chemical route under a N<sub>2</sub>-containing atmosphere and annealing of porous boron-containing precursors.<sup>20–22</sup> However, for the synthesis of BN nanoparticles of a spherical morphology, such methods are not widespread and the most developed approach is the CVD method. These days, spherical BN nanoparticles are in demand in many high-end applications in the fields of biology, medicine and ecology and one may expect that the areas of utilization of spherical BN nanoparticles will further be rapidly expanded due to their excellent physical and chemical properties.

Some synthetic methods of spherical BNNP production were already presented. For example, Tang *et al.*<sup>17</sup> reported high yield synthesis and detailed characterization of solid spherical BN nanoparticles with diameters of 50–400 nm, produced by a CVD reaction between B(OMe)<sub>3</sub> and ammonia at 980 °C, followed by high-temperature annealing at 1400 °C. The authors discussed the origin of oxygen impurities in BN nanoparticles and their influence on the morphology.

A two-step synthesis method of solid spherical BN particles with a size distribution from 50 to 400 nm was described

<sup>a</sup> National University of Science and Technology “MISIS”, Leninskiy prospect 4, Moscow, 119049, Russian Federation. E-mail: andreykovalskii@gmail.com, shtansky@shs.misis.ru

<sup>b</sup> Laboratoire CRISMAT, UMR 6508, CNRS-ENSICAEN, 6 Bd Marechal Juin, Caen, 14050, France

<sup>c</sup> International Center for Materials Nanoarchitectonics (MANA), National Institute for Materials Science (NIMS), Namiki 1-1, Tsukuba, Ibaraki, 3050044, Japan. E-mail: golberg.dmitri@nims.go.jp

† Electronic supplementary information (ESI) available. See DOI: 10.1039/c6ce01126h

by the same group.<sup>18</sup> The method combines the processes of chemical vapour deposition ( $T = 700\text{ }^{\circ}\text{C}$ ) and pyrolysis ( $T = 1100\text{ }^{\circ}\text{C}$ ) of trimethoxyborane under an ammonia atmosphere. According to chemical composition and high-resolution TEM analyses, BN particles had exhibited a slightly distorted arrangement of the shells. In addition, TEM and XRD observations suggested their partial disordering.

Spherical BN nanoparticles were also synthesized through the reaction of boric acid and ammonium chloride at  $T = 950\text{ }^{\circ}\text{C}$  under an  $\text{N}_2$  atmosphere.<sup>23</sup> A certain amount of copper oxide was crucial for the formation of uniform BNNPs with an average size of 30 nm. Hollow BN nanocages and BN-nanocage-encapsulated GaN nanocrystals were fabricated by using a B-N-O precursor at  $1750\text{ }^{\circ}\text{C}$  under Ar and  $\text{NH}_3$  flows.<sup>24</sup> B-N-O precursors were also proved to be effective sources of boron for the preparation of BNNTs and BN nanocages. The high yield synthesis of solid  $\text{BN}_x\text{O}_y\text{C}_z$  spherical particles with smooth and “crumpled aluminum foil ball” surfaces was reported.<sup>25,26</sup> The authors suggested that the reaction of gaseous ammonia with aerosol droplets of organoborate  $(\text{MeO})_3\text{B}$  suspended in nitrogen in a flight tube heated to  $800\text{--}1600\text{ }^{\circ}\text{C}$  had produced non-agglomerated spheres with a size of  $0.5\text{--}2\text{ }\mu\text{m}$  “dusted” with fine particles of  $100\text{--}150\text{ nm}$  in diameter. Chen *et al.*<sup>27</sup> developed an approach to prepare smooth hollow BN nanospheres *via* the reaction of  $\text{NaNH}_2$  and  $\text{BBr}_3$  at room temperature. These authors synthesized agglomerates of h-BN hollow spheres with a diameter between 80 and 300 nm and proposed that  $\text{BBr}_3$  droplets had served as templates for the sphere growth. The synthesis of nanosheet-structured BN by a catalyzing thermal evaporation method from solid B powders was also illustrated in ref. 28. Spheres of 700 nm to  $4\text{ }\mu\text{m}$  in diameter that formed only at a certain reaction temperature were made of radially oriented ultrathin nanosheets with their edges protruding from the sphere surfaces. The authors demonstrated the high potential of using such structures for water cleaning.

Hollow spherical BN nanoparticles of  $100\text{--}200\text{ nm}$  in diameter with petal-like surfaces were fabricated by a CVD method using boron oxide vapour and flowing ammonia.<sup>6</sup> The structural investigations demonstrated that the surface of the particles was made of numerous nanosheet petals. The capability of utilizing such structures as antitumor cells was additionally shown.

Several models were proposed to explain the formation mechanism of spherical BN nanoparticles. It was considered<sup>18</sup> that the presence of initial spherical particles in the precursors is essential for the creation of a spherical morphology in BN nanoparticles independent of the precursor chemical composition for the systems: B-N-O,<sup>18</sup> B-N-O-H<sup>25</sup> and  $\text{B}_2\text{O}_3\text{-BN}$ .<sup>29</sup>

Zhong *et al.*<sup>30</sup> suggested a mechanism of hollow BN nanoparticle formation relying on the decomposition of ammonia borane ( $\text{NH}_3\text{BH}_3$ ) at  $300\text{ }^{\circ}\text{C}$  and formation of gaseous phases containing B, N and H. These gases could flow into a high-temperature reaction zone where they react with each other

and condense into the BNH liquid droplets. After the particle diameters had exceeded a certain critical size, the BNH droplets in the vapour phase deposited onto an  $\text{Al}_2\text{O}_3$  substrate due to the gravitational effect. With an increase in temperature, the viscous BNH solid nanospheres undergo a dehydrogenation process which results in the appearance of small bubbles within the spheres. The bubbles tend to merge together under the surface tension of the viscous matrix, leading to the formation of final BN hollow nanospheres.

A model for the formation of solid spherical BN nanoparticles was proposed by Tang *et al.*<sup>17</sup> Reaction of trimethoxyborane  $\text{B}(\text{OMe})_3$  and ammonium led to the creation of spherical  $\text{B}(\text{OMe})_{3-x}\text{H}_{3-x}\text{N}$  intermediates which then transform into solid BN particles through decomposition and diffusion processes of gaseous by-products at high temperatures.

The current interest in spherical BN nanoparticles stems from a demand for obtaining homogeneously structured discrete spherical nanoparticles in large amounts for multi-functional applications. However, the development of an effective synthetic technique is still a great challenge. Since it was shown that the boron oxide-assisted CVD technique (BOCVD) is the most effective approach for the preparation of various BN nanomaterials, we thoroughly studied this method for the controlled fabrication of versatile BN nanoparticles.

Thus, in the present work we analyzed the growth of spherical BN nanoparticles of various morphologies during the BOCVD process under varying experimental conditions, namely, precursor composition, temperature, carrier and reactant gas flow rates and synthesis time. The morphology, structure, chemical composition and nanoparticle size distribution were studied in detail and peculiar growth mechanisms for each particle type were uncovered.

## 2. Experimental methods

### 2.1. Experimental set-up

Synthesis of BN nanoparticles was carried out using a vertical CVD induction system operating at  $41.4\text{ kHz}$ . The experimental set-up is shown in Fig. 1. The CVD system consists of a quartz cylindrical chamber, a cylindrical graphite heater (susceptor), a cylindrical reactor made of BN ceramics, a gas supply and an exhaust system. Ammonia was introduced to the BN reactor from the top, and argon was supplied from the bottom of the furnace. The heater was isolated from the quartz chamber by a low-density material made of carbon fibers. The temperature gradient (the scale on the right-hand side of Fig. 1), was monitored by using a W-Re thermocouple (A type) introduced in-between the heater and the thermal insulation, and a pyrometer was focused on the bottom of a crucible with precursors through a hole in the BN reactor bottom. This gradient can be varied by adjusting the relative positions of the inductor and the BN reactor.

The BN reactor consisted of three cylindrical parts with external and internal diameters of 75 and 55 mm, respectively,

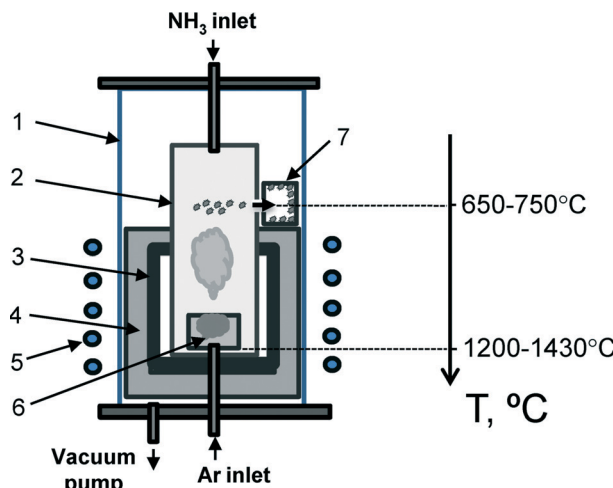


**Fig. 1** Scheme of the BOCVD system for spherical BNO nanoparticle synthesis. The equipment configuration: 1 –  $\text{SiO}_2$  furnace chamber, 2 – BN-reactor, 3 – graphite susceptor (heating element), 4 – graphitic thermal insulation, 5 – inductor, 6 – precursor crucible, and 7 – BNO-NP collecting crucible. Gas flows:  $\text{NH}_3$  (from the top) and Ar (from the bottom). The experimentally measured temperature profile along the reactor height is shown on the right.

and a total height of 340 mm. Its height was more than the height of the heater by approximately 30% to achieve a significant temperature gradient (Fig. 1). Initially, the temperature profile along the reactor was measured using an external thermocouple. The reactor (2) had a hole of 3 mm in diameter in its upper side wall part. A BN ceramic crucible (7) was placed in front of this hole for collecting nanoparticles transported from the BN reactor by a gas flow. Another BN crucible with a precursor (6) was placed at the bottom of the reactor, just above the argon inlet hole. The lower part of the reactor with the precursor was filled with argon and called hereafter the “argon zone”. Above the “argon zone” was the zone where ammonia is present. This zone is called the “ammonia zone”.

The furnace chamber was evacuated up to  $10^{-2}$  mbar under slow heating to 360 °C for outgassing of the low density graphitic thermal insulation. Then, an argon flow was introduced, the pressure of 1 bar was maintained, and heating to the synthesis temperature was started; this took about 15–18 min. At 1100 °C, an ammonia flow was introduced. The precursor temperature (synthesis temperature) was varied in the range of 1200–1430 °C. The ammonia flow was set in the range of  $30\text{--}150 \text{ cm}^3 \text{ min}^{-1}$ , and the Ar/ $\text{NH}_3$  flow ratio was maintained from 2 to 6. The syntheses were carried out for 3–7 hours. After the synthesis, the reactor was naturally cooled to room temperature under argon.

## 2.2. Materials

Powder mixtures of B, MgO,  $\text{H}_3\text{BO}_3$ , FeO or SnO were used as the precursors. Three types of mixtures were tested as a source of boron oxide vapour, *i.e.* FeO + MgO + B, SnO + MgO + B

**Table 1** Chemical compositions of precursor powder mixtures for BOCVD syntheses

Mixture no.	Molar ratio of chemicals				
	B	MgO	FeO	SnO	$\text{H}_3\text{BO}_3$
1	3.5	1.25	1	—	—
2	3.5	0.1	1	—	—
3	3.5	0.2	1	—	—
4	1	1	—	1	—
5	3.5	0.1	—	1	—
6	3.5	0.2	—	—	2.6

and  $\text{H}_3\text{BO}_3 + \text{MgO} + \text{B}$ . The molar ratios of chemicals in the precursor powder mixtures are presented in Table 1.

Reagents of the following grades: MgO – analytical grade, amorphous B – >99%, FeO – pure, SnO – 99%,  $\text{H}_3\text{BO}_3$  – chemical grade. Magnesia was calcined at 450 °C in air for 1 h for dehydration just before weighing.

Precursor mixtures were mechanically ground in a mechanical alumina mortar for 1 h with addition of isopropyl alcohol. Argon of 99.993% purity was used as the carrier gas and ammonia of 99.98% purity was used as the reactant gas.

## 2.3. Characterization

The morphologies of the synthesized products and their elemental compositions were analyzed using a scanning electron microscope (JSM-7600F) (JEOL) equipped with an energy-dispersive X-ray (EDX) detector.

Transmission electron microscopy (TEM) and electron diffraction (ED) studies were performed using a Tecnai G2 30 UT ( $\text{LaB}_6$ ) microscope operated at 300 kV with a 0.17 nm spatial resolution and equipped with an EDAX EDX detector. High-angle annular dark field (HAADF) scanning TEM (STEM) imaging and EDX elemental mapping were performed using a JEM ARM200F cold field emission gun (FEG) probe and an image aberration-corrected electron microscope operated at 200 kV, equipped with a large solid-angle CENTURIO EDX detector and a Quantum GIF. The powder samples for TEM were ground in methanol, and the resulting dispersion was transferred to a holey carbon film deposited on a Cu supported grid.

The chemical and phase compositions were investigated by EDX spectroscopy using an 80 mm<sup>2</sup> X-Max EDX detector (Oxford Instruments), confocal Raman spectroscopy using an NT-MDT NTEGRA Spectra instrument with an excitation wavelength of 473 nm, X-ray diffraction analysis using a DRON-3 diffractometer (Burevestnik) operated with  $\text{Cu K}\alpha$  radiation and Fourier-transform infrared spectroscopy (FTIR) using a Vertex 70v vacuum spectrometer (Bruker) in the range of 400–2000 cm<sup>-1</sup> using a partial internal reflection device. In order to separate the agglomerates into discrete individual BNO-NPs, they were ultrasonically treated in a distilled water solution (nanoparticle concentration: 2 mg ml<sup>-1</sup>) employing a Sonoplus HD2200 unit (Bandelin) at a power of 80 W for 30 min. To control the spherical nanoparticle sizes and the homogeneity of size distribution, parallel studies using the

dynamic light scattering method were performed by means of a particle size analyzer (Zetasizer Nano ZS) (Malvern Instruments), while utilizing the SEM method.

### 3. Results

After each synthesis, a thin white-colored deposit was observed on the inner surface of the BN reactor and in the collecting crucible (Fig. S1(a) in the ESI<sup>†</sup>). Typically, 250–400 mg of the white material was obtained in the BN crucible, from 10 g of the precursor after a 7 h process. When the Ar/NH<sub>3</sub> flow ratio was less than 4, a white powder also covered the precursor surface, as shown in Fig. S1(b) in the ESI<sup>†</sup>. In this case, the traces of outgassing were seen in this newly formed material.

The X-ray diffraction patterns of the synthesized materials obtained from various precursors were very close to that of a hexagonal BN phase (Fig. S2 in the ESI<sup>†</sup>). The XRD pattern of h-BN (COD card No. 96-900-8998; cell parameters  $a = 2.5040 \text{ \AA}$ ,  $c = 6.6612 \text{ \AA}$ ) was used as a reference. The small shift of peak positions is associated with the slightly larger unit cell parameters due to the presence of a small amount of oxygen in the structures, as was also detected by FTIR and EDX analyses.

SEM investigations proved that the synthesized material consisted of nanoparticles of a spherical shape. EDX analysis (not shown here) confirmed that the nanoparticles generally consisted of B and N species with the atomic ratio B:N close to 1:1 and also showed the presence of oxygen in this sample.

The Raman spectra of the materials synthesized from different precursors display a clear band at 1368 cm<sup>-1</sup>, corresponding to the  $E_{2g}$  mode of a hexagonal BN. A typical Raman spectrum of a material obtained at 1300 °C from the H<sub>3</sub>BO<sub>3</sub> + MgO + B precursor is presented in Fig. S3 in the ESI<sup>†</sup>. A difference was found in the full width at half maximum (FWHM) values of the Raman peak. The FWHM was about 25 cm<sup>-1</sup> for the samples synthesized from the H<sub>3</sub>BO<sub>3</sub> + MgO + B precursor and about 40 cm<sup>-1</sup> for the samples synthesized from the FeO + MgO + B and SnO + MgO + B mixtures. Such narrowing of bands corresponds to an improvement in the overall sample crystallinity.

The FTIR spectra of the samples synthesized from different precursors are shown in Fig. 2. The FTIR spectrum recorded from the sample prepared from the FeO + MgO + B precursor included two main features: a sharp peak at 769 cm<sup>-1</sup> and a broad band at 1359 cm<sup>-1</sup> corresponding to out-of-plane B–N–B bending and in-plane B–N stretching vibrations, respectively.<sup>31</sup> These peaks are the fingerprints of the sp<sup>2</sup>-bonded BN. The FTIR spectrum of the sample synthesized from the H<sub>3</sub>BO<sub>3</sub> + MgO + B precursor had some additional features – broad zones with a high absorbance in the ranges of 400–720 cm<sup>-1</sup>, 850–1200 cm<sup>-1</sup>, and 3000–3500 cm<sup>-1</sup>. These features can be due to some amount of oxygen and/or O–H impurities,<sup>31,32</sup> these are apparently related to the usage of boric acid in this precursor and its evolution during the synthesis. Thus, from a comparison of Raman and FTIR data,

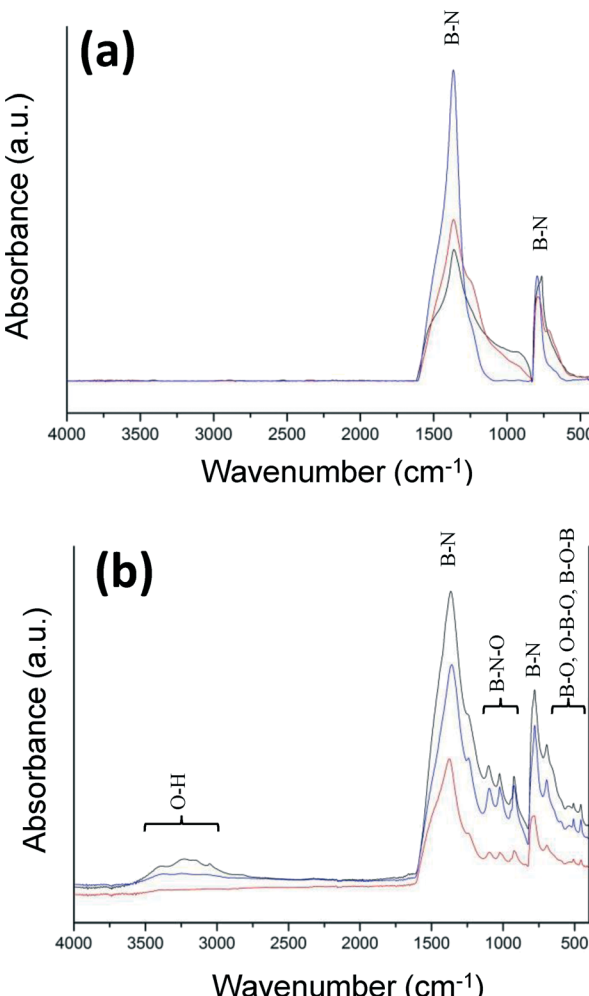


**Fig. 2** Comparative FTIR spectra of the materials obtained using various precursors: a) FeO + MgO + B and b) H<sub>3</sub>BO<sub>3</sub> + MgO + B. The representative B–N, B–N–O, B–O and O–H modes are marked.

one may conclude that oxygen somehow improves the crystallinity of BNO nanoparticles.

X-ray, FTIR, and EDX analyses evidenced that the synthesized materials are hexagonal boron nitrides with some oxygen contents; therefore, hereafter we name the synthesized products as boron oxynitride nanoparticles (BNO-NPs). The experimental conditions affected the oxygen contents in the products (to some extent) and the BNO-NP product yield. SEM analysis revealed that the BNO-NPs possess two major surface morphologies: smooth and petalled (Fig. 3(a) and (b)). The petals were made of numerous thin BNO nanosheets reminiscent of graphenes. Usually, spherical particles with smooth and petalled surfaces were found to coexist, whereas the latter morphology dominated. Some syntheses almost exclusively produced particles with petalled surfaces (with a yield of more than 90%). Nearly solely smooth surface nanospheres were observed only in a few experiments under certain synthesis conditions. The preferential fabrication of BNO-NPs with a distinct surface morphology could be controlled through selecting the

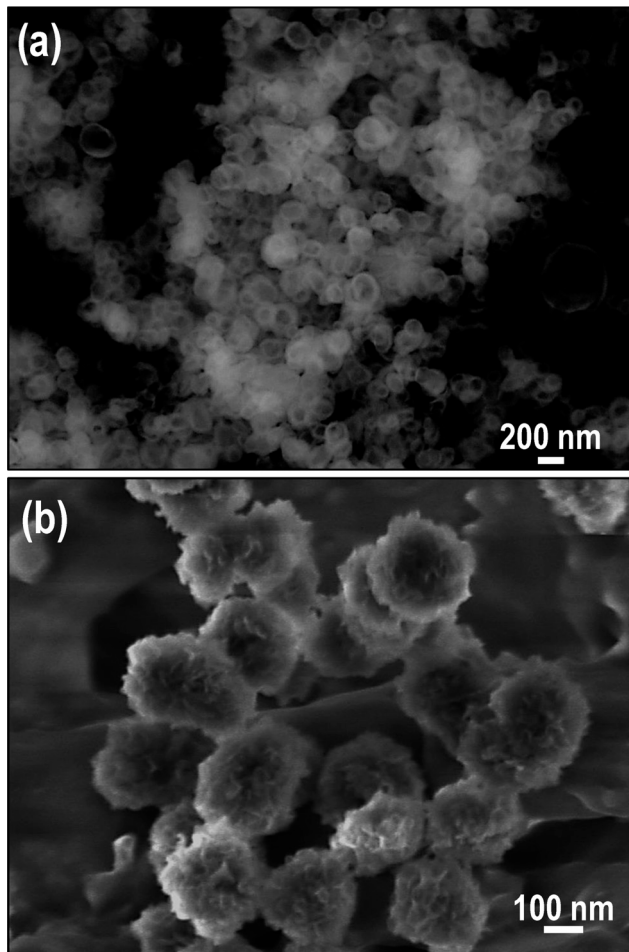


**Fig. 3** SEM images of spherical BNO-NPs: a) with a smooth surface obtained at 1310 °C from a FeO + MgO + B precursor and b) with a petalled surface obtained at 1410 °C from a SnO + MgO + B precursor.

precursor composition, gas atmosphere and flow rates of carrier and reactant gases.

Particle size distribution analysis showed that the BNO-NP size was in the range of 80–350 nm for all types of particles synthesized from various precursors. Both SEM and particle size distribution revealed that BNO-NPs became perfectly separated after the ultrasonic treatment. The procedures of ultrasonic treatment and particle size measurements were similar to those described in our earlier publication.<sup>6</sup>

Detailed TEM investigations allowed us to identify six major types of BNO-NP structures (Fig. 4): hollow or solid, with thick or thin shells and with smooth or petalled surfaces. The first type of structures (type I) was the solid “onion”-like particles with a smooth surface (Fig. 4(a)). The second type (type II) was the solid particles consisting of BN nanosheets forming “pompon”-like structures (Fig. 4(b)).

Other types of BNO-NPs were hollow. These types of particles may have a thin, almost regular spherical shell, or thick shells of both spherical and irregular shapes. BNO-NPs of type III are hollow structures of a spherical shape with a thin shell (shell thickness of 10–20 nm) and a smooth surface

(Fig. 4(c)). BNO-NPs of type IV are hollow spherical structures with a shell consisting of numerous large BNO nanosheets whose size is comparable with the diameter of the hollow core (Fig. 4(d)). BNO-NPs of type V are hollow structures with a smooth thick shell having a thickness comparable with the hollow core diameters (Fig. 4(e)). The hollow may be shifted from the center of the particle so that the particle walls become of a variable thickness. Sometimes this type of BNO-NPs contains two or more hollows. These nanoparticles often have an irregular shape. BNO-NPs of type VI are hollow structures with petalled thick shells, whose thickness is comparable with the hollow core diameters (Fig. 4(f)). The shells of these nanoparticles consist of two segments, *i.e.* the smooth inner domain and the outer petalled shield. The petals are less spacious in size but are more densely populated than in the case of type IV particles. In these particles, the hollows may also be out of the particle centers, like in type V particles.

The detailed HRTEM study was carried out for the BNO-NPs with two selective types of surface morphologies, namely with the smooth surfaces (types III and V) produced at 1310 °C from the FeO + MgO + B precursors and with the petalled surfaces (type IV) synthesized at 1245 °C from the SnO + MgO + B precursor. The TEM images (Fig. 5(a) and (b)) illustrate spherical BNO nanoparticles with a layered structure. The internal structure of the particles presented in the insets of Fig. 5(a) and (b) corresponds to a hexagonal BN with an interlayer spacing of 0.33 nm.

The results of TEM studies of BNO-NPs with the smooth surface are shown in Fig. 6(a) and (b). A bright-field image of nanoparticles with a size of around 80–100 nm and a smooth surface is presented in Fig. 6(a). The wall thickness is quite irregular being in the range of 20–35 nm. The light grey contrasts inside the particles suggest the lack of any solid fillings and the existence of hollow cores. The wall thickness remains the same (20–35 nm) even in larger particles, ~200 nm in size, although their inner diameter is significantly larger. To verify the BNO-NP local chemical compositions, EDX elemental mapping was performed (Fig. 6(d)–(f)). A HAADF-STEM image of BNO-NPs is depicted in Fig. 6(c). The contrast in a HAADF-STEM image is roughly proportional to the thickness of the specimen and to the square of the atomic number of the element ( $\sim Z^2$ ). Thus, HAADF-STEM imaging represents both chemically and thickness sensitive contrasts. In this respect, it is clear that the contrast in the HAADF-STEM image (Fig. 6(c)) is due to the thickness difference, thus unambiguously supporting the hollow structure of the BNO-NPs. The non-homogeneous contrast inside the large BNO-NPs is most probably related to the variable thickness of the particle shell. EDX mapping (Fig. 6(d)–(f)) confirms that the particles consist of B, N, O.

TEM observations of a sample with a petalled surface revealed more complex structures (Fig. 7). The surface of BNO-NPs consists of numerous BN petals. Such petals were previously observed in porous BN nanospheres.<sup>33</sup> SAED analysis confirmed that the petals are made of hexagonal BN (the

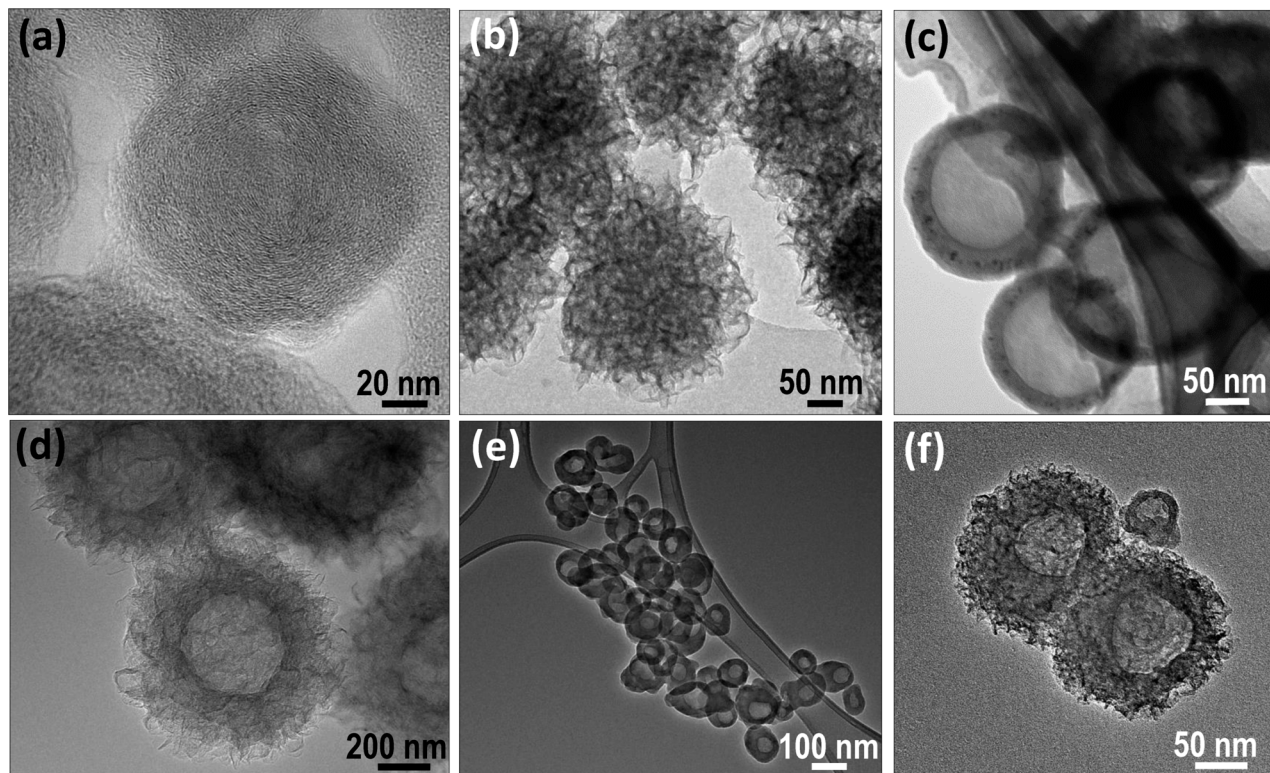


**Fig. 4** Bright-field TEM images of six types of spherical BNO-NPs of different morphologies and structures: a) solid “onion”-like particles with smooth surfaces (type I); b) solid “pompon”-like particles (type II); c) hollow thin-shelled particles with smooth surfaces (type III); d) hollow thin-shelled particles with petalled surfaces (type IV); e) hollow thick-shelled particles with smooth surfaces (type V); and f) hollow thick-shelled particles with petalled surfaces (type VI).

inset in Fig. 7(a)). Elemental mapping (Fig. 7(b)) showed that they consist of B, N, and O. HRTEM images (Fig. 7(c) and (d)) revealed the presence of stacked heavily curled and bent BNO nanosheets with a thickness of 3–4 nm. Similar BN nanosheets with thicknesses from 3.1 to 9.1 (depending on precursor composition) were observed on the spherical BN particles.<sup>28</sup> The lattice fringes corresponding to the typical d-spacing of h-BN viewed along two orthogonal ([1010] and [0001]) projections are clearly seen on the HRTEM images. The EEL spectra of this sample are presented in Fig. S4 in the ESI.† The spectra of the central region and the near-surface region (shell) of the nanoparticle were similar and corresponded to the h-BN structure.

To sum up, in accordance with our thorough structural and morphological analyses, six different types of BNO-NPs with smooth or petalled surfaces were identified: four types having hollow morphologies and two types with solid cores, *e.g.* “onion”-like and “pompon”-like particles (Fig. 4).

## 4. Analysis and discussion

According to the existing literature, various spherical BN nanoparticles, *i.e.* hollow and solid, with smooth or petalled surfaces can be synthesized by means of different methods. Generally, one method produces one type (or rarely a few types) of BN nanospheres. Only the applied BOCVD method

based on the reaction of ammonia with boron oxide vapour generated during the thermal decomposition of the boron-oxide precursor has an advantage of producing a variety of spherical BN-based nanoparticles. Our systematic investigation of the presently utilized BOCVD process allowed us to propose a more general model of spherical BN-based particle formation. Below, we consecutively analyze the different stages of the physical-chemical processes.

### 4.1. Processes in the precursor

Two types of B sources in the precursors were tested, *i.e.* boron oxide-based ( $(B_2O_3 + BN)$  and  $(MgO + n \cdot B_2O_3)$ ) and elemental boron-based – ( $B + B_2O_3$ ), ( $B + MgO + FeO$ ), and ( $B + MgO + SnO$ ). Under heating of the first precursor type, boron oxide is melted with the formation of borates, for example, Mg borate in the case of using MgO. The volatile fractions of boron oxide compounds (BOC) are vaporized. The kinetics of this process depends on the temperature and precursor composition (Fig. 8, stage a). In the case of using heterogeneous precursors consisting of liquid and solid phases at high temperature, in addition to surface vaporization, vaporization also occurs from the liquid–solid interfaces enhancing the overall vaporization kinetics. In addition to vaporization, bubbling is also possible if the liquid surface tension is high enough. This also depends on the melt composition and temperature. The essential condition for bubble formation is the

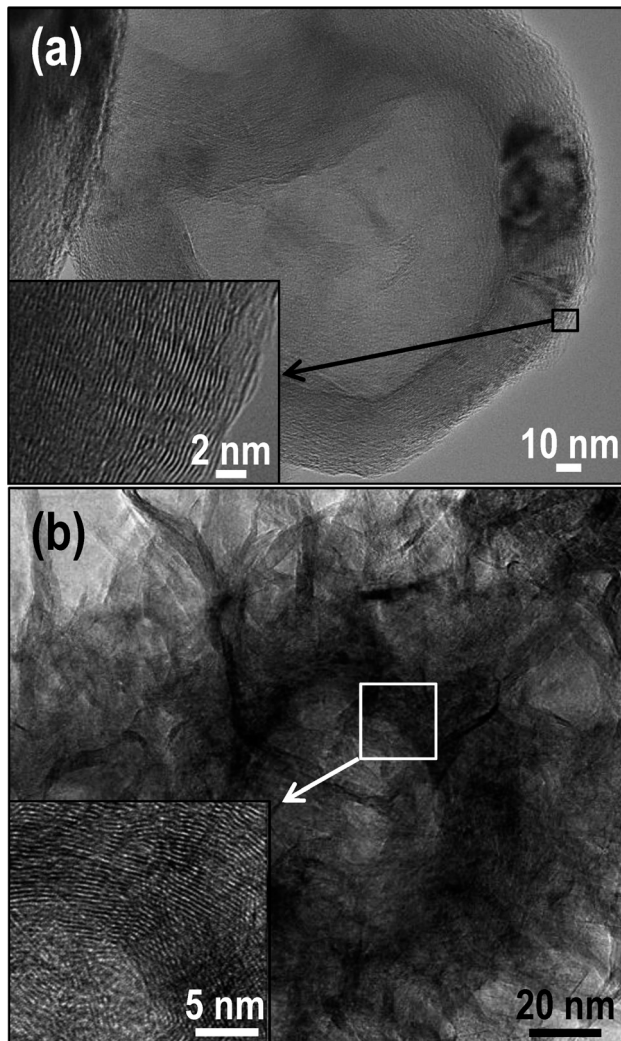


**Fig. 5** Bright-field TEM images of hollow BNO-NPs: a) with a smooth surface (type III) and b) with a petalled surface (type IV). The insets show bright-field aberration-corrected HRTEM images of a layered structure within the respective types of spherical BNO-NPs.

presence of a solid-phase particle in the melt. The latter plays the role of a frame for liquid film formation similar to soap bubbling. It is known that boron oxide-based melts have a high ability to form films and foams due to a polymeric nature of (-B-O-) bonds. Increasing the melt temperature leads to a decrease in its viscosity, resulting in bubble wall thinning (Fig. 8, stage b). By contrast, if the temperature is not high enough, thick-walled bubbles appear (Fig. 8, stage c). Increasing the MgO content in the precursor (more than 50% mol) favours thick-walled bubbles due to the formation of refractory Mg borates. The higher the Ar flow rate over the precursor, the faster the vaporization and bubbling took place due to a decrease in partial vapour pressure above the melt and in the overall pressure, according to the Bernoulli law.

Under heating of the B-containing precursor, its oxidation occurs, as described by the following chemical reactions:

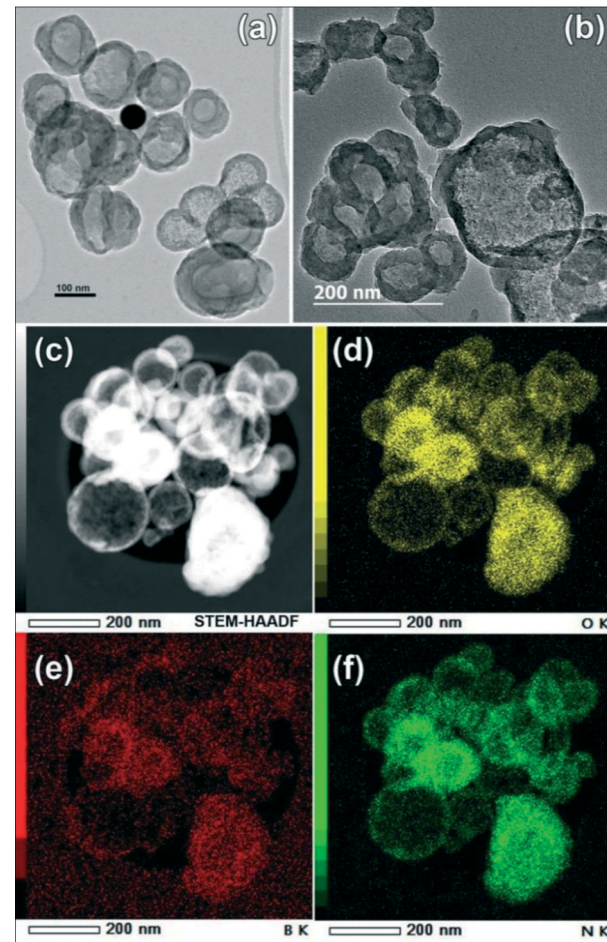
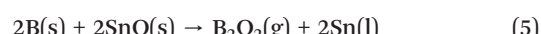
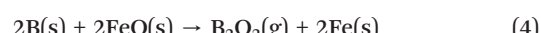
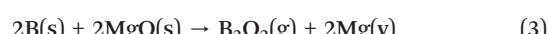


**Fig. 6** (a) and (b) Bright-field TEM images of hollow BNO-NPs of different sizes and morphologies obtained at  $T = 1310$  °C from the  $\text{FeO} + \text{MgO} + \text{B}$  precursor; (c) a HAADF-STEM image of BNO-NPs. The corresponding EDX maps show the spatially-resolved elemental distribution of O (d), B (e), and N (f).



In this case, the above-mentioned arguments remain valid because boron and metal oxides are still present in the melts.

In addition to boron oxide and borate vapours, the volatile  $\text{B}_2\text{O}_2$  oxide forms, as described by the redox reactions:<sup>34</sup>



Briefly, vapours of BOC and thin or thick shell BOC bubbles form in this zone, depending on the temperature and precursor composition.

#### 4.2. Processes above the precursor (zone of argon)

This zone is marked as Ar in Fig. 8. Its size depends on the  $\text{Ar}/\text{NH}_3$  flow rate ratios and increases with an increase in the

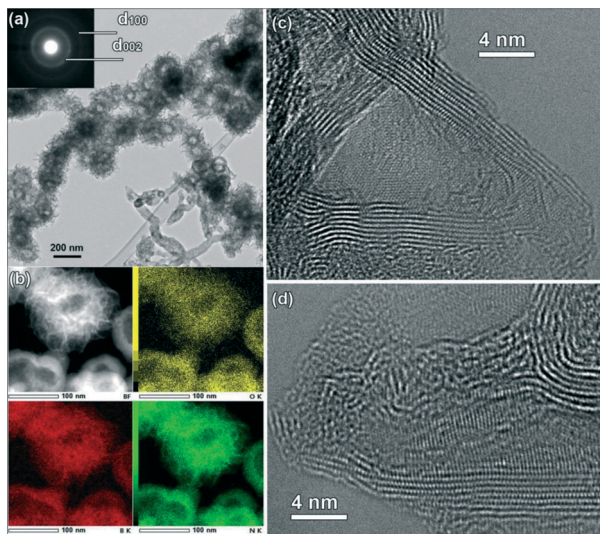


**Fig. 7** a) A bright-field low-magnification TEM image and the corresponding ring ED pattern of hollow BNO-NPs with petalled surfaces obtained at 1245 °C from the SnO + MgO + B precursor; b) HAADF-STEM image together with the spatially-resolved EDX elemental maps (O-yellow, B-red, N-green); c) and d) bright-field aberration-corrected HRTEM images of BNO petals on hollow BNO-NPs.

Ar flow rate. In this zone, BOC vapours start to cool down and their condensation takes place if the vapour concentration is high enough. At sufficiently low pressure, BOC vapour condensation does not occur (Fig. 8, stage e). Under a high concentration of vapours, condensation leads to the formation of a tiny mist of liquid BOC droplets (yellow circles in Fig. 8). The droplet collisions lead to their enlargement and formation of BOC solid nanoparticles (Fig. 8, stage d), whereas the impact of droplets with bubbles results in an increase in bubble wall thicknesses (Fig. 8, stage f). The probability of such collisions is proportional to the Ar flow speed; the faster the speed, the greater is the flow turbulence. Under a large vertical temperature gradient, the viscosity of a boron-oxide melt within the bubbles and droplets quickly increases during its upward propagation. This hinders the coalescence of the droplets and bubbles and leads to the formation of irregularly-shaped particles (Fig. 8, stage f).

Briefly, the condensation of vapours, the formation of tiny BOC droplets and the coalescence of the droplets occur in this zone.

#### 4.3. Processes in the ammonia zone

This zone is marked as NH<sub>3</sub> in Fig. 8. In this zone, the BOC vapour, ammonia and either hollow or solid nanoparticles pre-formed in the lower Ar zone are all present. Here, the temperature continues to decrease and the BN-based phase is formed as a result of B-oxide reactions with ammonia with the release of water vapour, as described by the following reaction:



The kinetics of this reaction depends on the temperature and ammonia concentration and influences the morphology of the final BNO products. If the ammonia concentration is low, while the temperature is high, the volume of formed BN (and water) is not large, whereas the diffusion rate is fast. Under such conditions, a water vapour easily diffuses out of the particles without breaking them, and the “onion”-like structures with smooth surfaces or thin- and thick-walled smooth particles are formed (types I, III and V). An analogous mechanism was considered by Tang *et al.*<sup>17</sup> during a reaction of trimethoxyborane with ammonia, elimination of gaseous MeOH & Me<sub>2</sub>O without losing the particle integrity, and the formation of solid spheres.

Under the opposite conditions, *i.e.* a high ammonia concentration and a relatively low temperature, the volume of the released water vapour is increasing, while its diffusion rate within the particle volume is decreased. Thus, the water vapour does not succeed in entirely penetrating through the growing BN layers, leading to inner pressure growth and resultant BNO shell breakage. As a result, BNO nanoparticles with highly developed surfaces covered with numerous graphene-like BN petals appear. The size of the petals and their amount depend on the defectiveness of the BOC particles. Surface defects and inhomogeneities within these particles lead to a decreased petal size and an increase in their density on surfaces. Nanostructures of type VI (Fig. 8) are formed in this scenario from the hollow irregularly-shaped BOC. Hollow smooth BOC particles of the right spherical form exhibit lesser defects, meaning that a small amount of spacious petals emerge on their surface. In the case of thin-walled spheres, these processes sometimes result in the complete vanishing of shells, leaving particles with a crown-like appearance of petals. Upon further development of these structures, type IV particles are crystallized; these have petals with a size comparable to their overall diameters. In the case of solid (without hollow) BOC nanoparticles, the processes of formation and breakage of BNO layers propagate inward, forming spherical particles made of numerous packed petals. Upon further growth, these transform to “pompon”-like particles, the type II structure.

At the same time, a CVD process based on the reaction of ammonia with BOC vapours adsorbed on the newly formed BNO surface takes place. As a result, graphene-like BNO petals substantially grow in linear dimensions, creating large surface flakes, like in the case of the type IV morphology. They are easily bent – making numerous folds. These stimulate intense condensation of BOC vapours. The condensate readily reacts with ammonia, leading to the nucleation and growth of new BNO sheets and producing dense and thick BNO coats, as in the case of II, IV, and VI morphologies.

To summarize, in this zone, adsorption, condensation, and reaction of BOC with ammonia occur, leading to the formation of BNO nanosheets and growth of both their size and amount.

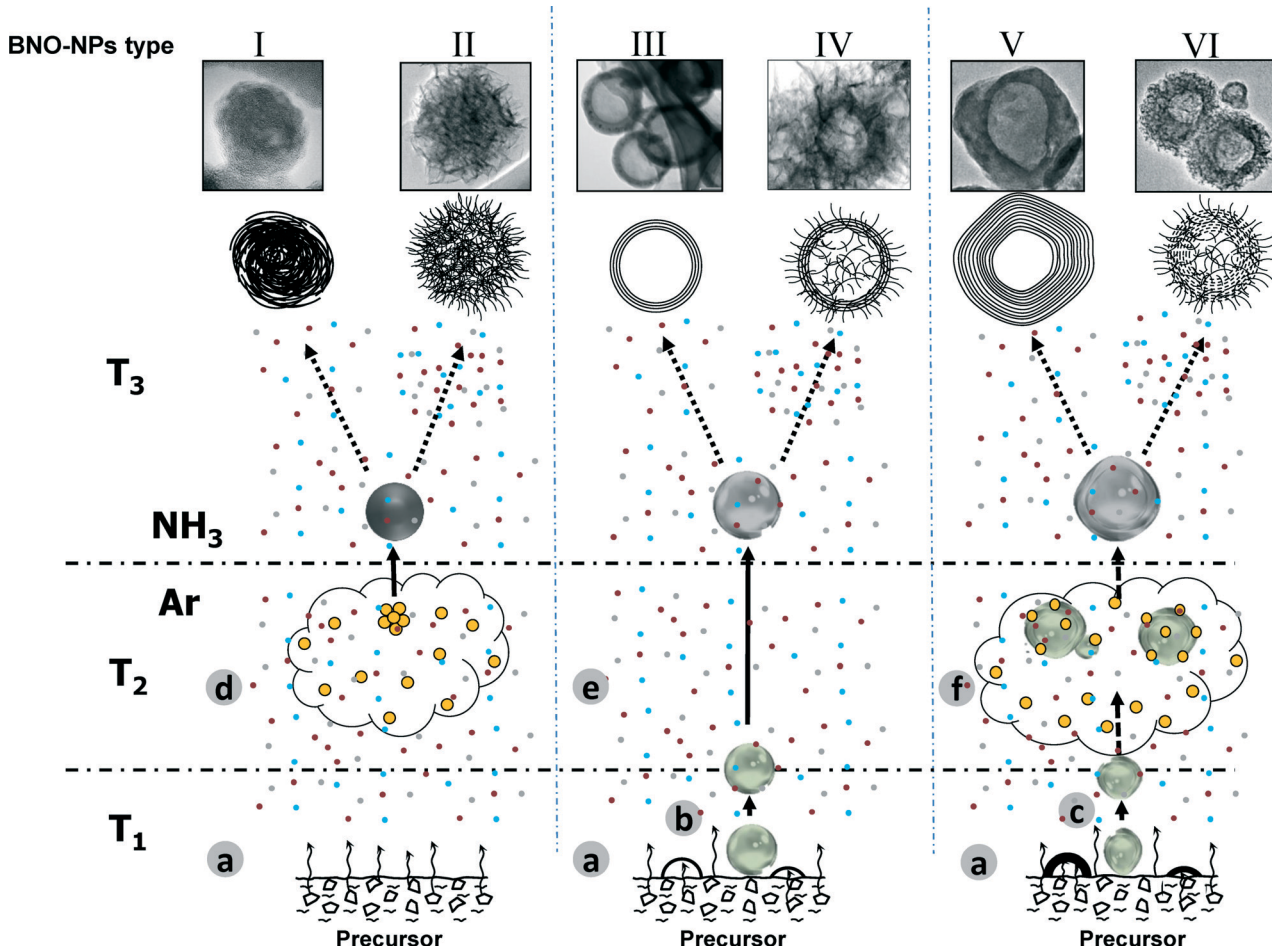


**Fig. 8** A model for the formation of six BNO-NP types, including the following stages: a) evaporation of fugitive BOC from the precursor, b) thin-shelled borate bubble formation, c) thick-shelled borate bubble formation, d) formation of a mist of tiny BOC liquid droplets and their collision leading to the formation of solid BOC particles, e) low concentration vapours of BOC, f) collision of tiny liquid droplets of BOC and borate bubbles resulted in an increase in shell thickness. The temperature gradient corresponds to  $T_1 > T_2 > T_3$ . Colour codes: red, blue and grey dots – vapours of BOC, yellow dots – condensed droplets.

#### 4.4. Formation of nanoparticles of a specific morphology

It is worth noting that obtaining particles of totally identical morphology in a given synthetic run is not always possible, as the conditions for the synthesis of some nanoparticles are nearly analogous. As a result, occasionally, a mixture of various morphologies may be found in a product, as depicted in Fig. 9(a). The general condition for all structure formations is an intense vaporization of BOCs.  $B_2O_3$  does satisfy this criterion, since it has a low vapour pressure under 1200 °C. In addition, we note that boron anhydride has substantially slower kinetics of interaction with ammonia than borates of rare and rare-earth metals containing some amount of oxide-forming borate.<sup>35,36</sup> Among all precursors studied in the present work, a mixture of ( $B + B_2O_3$ ), forming a volatile  $B_2O_2$ , and precursors in which Mg borates with a relatively low MgO concentration (<50% mol) are present, satisfy the said criteria. For the synthesis of “onion”-like structures (type I), a high temperature, a fast Ar flow and a low concentration of ammonia are advantageous. Under similar conditions, but at

a higher ammonia concentration, “pompon”-like morphologies (type II) would form. For the production of hollow particles, ( $B + B_2O_3$ ), ( $B + MgO + FeO$ ), ( $B + MgO + SnO$ ) and ( $MgO + n \cdot B_2O_3$ ) precursors, which at a high temperature consist of liquid and solid phases (B, Fe, MgO, and  $Mg_2B_2O_5$ ), are required. A high temperature in the precursor zone and in the ammonia zone, but a low ammonia concentration, promotes the formation of thin-walled particles (type III). Increasing the ammonia concentration and a larger temperature gradient along the reactor lead to the formation of surface BNO petals on hollow particles (type IV and VI) or “pompon”-like morphologies (type II). Decreasing the temperature in the precursor zone and the ammonia concentration, while increasing the Ar flow, stimulates the formation of hollow particles with smooth thick shells (regular and irregular shapes) (type V). Table 2 qualitatively summarizes the reaction conditions favouring the formation of different particle morphologies.

The above analysis implies that the formation of BOC bubbles from a precursor melt and the development of their

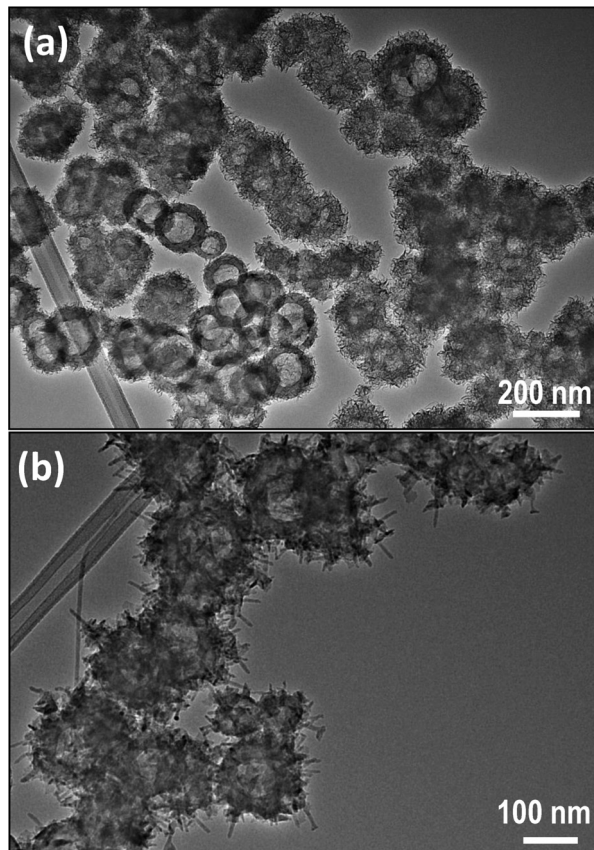


**Fig. 9** a) Bright-field TEM image of spherical BNO-NPs in a material obtained in a single synthetic run. Nanoparticles of types II, III, IV, and VI and their modifications are apparent. b) Bright-field TEM image of a new type of spherical BNO-NPs of a “hedgehog” morphology with BN nanowires on the surfaces.

**Table 2** Experimental parameters favouring the formation of different particle morphology types

Type of BNO-NPs	Precursor composition enabling BOC bubble formation	Temperature in the precursor zone <sup>a</sup>	Temperature in the ammonia zone <sup>b</sup>	Ar flow rate <sup>c</sup>	NH <sub>3</sub> flow rate <sup>d</sup>
I	No	High	Low	High	Low
II	No	Low	Low	Low	High
III	Yes	High	High	High	Low
IV	Yes	High	Low	Low	High
V	Yes	Low	Low	High	Low
VI	Yes	High	Low	Low	High

<sup>a</sup> In the range of 1200–1430 °C. <sup>b</sup> In the range of 650–750 °C. <sup>c</sup> In the range of 180–500 cm<sup>3</sup> min<sup>-1</sup>. <sup>d</sup> In the range of 30–150 cm<sup>3</sup> min<sup>-1</sup>.

surface through condensation or adsorption of BOC vapours under reaction with ammonia is the crucial stage of specific morphology crystallization. To prove the validity of this claim, an additional test experiment was undertaken. 0.5 wt% of Li<sub>2</sub>O was added to the (B + MgO + FeO) precursor and the synthesis was carried out under the conditions when hollow smooth BNO thick-walled particles were formed without

such addition. Under heating of the new precursor, lithium borate having both low melting point and high volatility should form, thus in the frame of the proposed model, Li borate should crystallize on the BOC surfaces in the ammonia zone. This should change the resultant morphology. In fact, Fig. 9(b) illustrates the formation of new “hedgehog”-like particles covered with BN nanowires. Importantly enough, in our recent work<sup>36</sup> we have concluded that BN nanotubes and nanowires preferentially nucleate and grow from a Li borate-based melt. Therefore, the formation of surface-attached BN nanowires on smooth spherical BNO-NPs indicates the predicted condensation of Li borate vapours followed by this condensate reaction with ammonia, in accordance with the developed model.

## 5. Conclusions

Six types of spherical BNO nanoparticles with external dimensions of 80–350 nm and having hollow and solid cores, and smooth and petalled surfaces (with numerous thin-walled BN petals) were synthesized using three kinds of precursor compositions, *i.e.* FeO + MgO + B, SnO + MgO + B and H<sub>3</sub>BO<sub>3</sub> + MgO + B at 1200–1430 °C using a CVD approach. BNO-NPs were obtained as homogeneously structured agglomerates. Changing the experimental conditions affects the particle morphology, oxygen content and the product yield. The structures and morphologies of various BNO-NPs were analyzed in detail and the particular mechanism for each particle morphology appearance was uncovered. BNO-NPs of a new “hedgehog” morphology with surface-attached BN nanowires were first predicted and then synthesized in the test experiment in accordance with the model. We envisaged that the present research would be highly valuable in the field of BN nanomaterial fabrication and their utilization in diverse industrial fields.

## Acknowledgements

This work was partially supported by the Ministry of Education and Science of the Russian Federation (Increase Competitiveness Program of NUST “MISiS” No. K2-2015-001 and State task 11.1077.2014/K) and the Russian Foundation for Basic Research Grant No. 16-08-00957/16. We are also grateful to S. Turner for his help with EELS measurements. D. G. also acknowledges MANA-NIMS for a support.

## References

- 1 J. J. Pouch, *Synthesis and properties of boron nitride*. Materials Science Forum; Trans, Tech Aedermannsdorf, Switzerland, 1990.
- 2 C. Y. Zhi, Y. Bando, C. C. Tang, R. G. Xie, T. Sekiguchi and D. Golberg, *J. Am. Chem. Soc.*, 2005, 127, 15996.
- 3 X. X. Yang, Z. X. Guan, M. Zeng, J. K. Wei, W. L. Wang and X. D. Bai, *Small*, 2013, 9, 1353.

- 4 C. Y. Zhi, N. Hanagata, Y. Bando and D. Golberg, *Chem. - Asian J.*, 2011, **6**, 2530.
- 5 R. T. Paine and C. K. Narula, *Chem. Rev.*, 1990, **90**, 73.
- 6 I. V. Sukhorukova, I. Y. Zhitnyak, A. M. Kovalskii, A. T. Matveev, O. I. Lebedev, X. Li, N. A. Gloushankova, D. Golberg and D. V. Shtansky, *ACS Appl. Mater. Interfaces*, 2015, **7**, 17217.
- 7 M. Sajjad, G. Morell and P. Feng, *ACS Appl. Mater. Interfaces*, 2013, **5**(11), 5051.
- 8 Y. M. Zhang, X. D. He, J. C. Han and S. Y. Du, *J. Mater. Process. Technol.*, 2001, **116**, 161.
- 9 S. J. Zhou, C. Y. Ma, Y. Y. Meng, H. F. Su, Z. Zhu, S. L. Deng and S. Y. Xie, *Nanotechnology*, 2012, **23**, 055708.
- 10 J. Yu, L. Qin, Y. F. Hao, S. S. Kuang, X. D. Bai, Y. M. Chong, W. J. Zhang and E. G. Wang, *ACS Nano*, 2010, **4**, 414.
- 11 H. Zhao, J. Song, X. Song, Z. Yan and H. Zeng, *J. Mater. Chem. A*, 2015, **3**, 6679.
- 12 Q. H. Weng, X. B. Wang, C. Y. Zhi, Y. Bando and D. Golberg, *ACS Nano*, 2013, **7**, 1558.
- 13 C. Zhi, Y. Bando, C. Tan and D. Golberg, *Solid State Commun.*, 2005, **135**, 67.
- 14 S. Bernard, V. Salle, J. Li, A. Brioude, M. Bechelany, U. B. Demirci and P. Miele, *J. Mater. Chem.*, 2011, **21**, 8694.
- 15 T. Oku, T. Kusunose, K. Niihara and K. Suganuma, *J. Mater. Chem.*, 2000, **10**, 255.
- 16 Y. Qiu, J. Yu, J. Yin, C. Tan, X. Zhoul, X. Bai and E. Wang, *Nanotechnology*, 2009, **20**, 345603.
- 17 C. Tang, Y. Bando, Y. Huang, C. Zhi and D. Golberg, *Adv. Funct. Mater.*, 2008, **18**, 3653.
- 18 C. Tang, Y. Bando and D. Golberg, *Chem. Commun.*, 2002, 2826.
- 19 S.-K. Kim, H. Cho, M. J. Kim, H.-J. Lee, J. Park, Y.-B. Lee, H. C. Kim, C. W. Yoon, S. W. Nam and S. O. Kang, *J. Mater. Chem. A*, 2013, **1**, 1976.
- 20 A. Fathalizadeh, T. Pham, W. Mickelson and A. Zettl, *Nano Lett.*, 2014, **14**, 4881.
- 21 K. S. Kim, C. T. Kingston, A. Hrdina, M. B. Jakubinek, J. Guan, M. Plunkett and B. Simard, *ACS Nano*, 2014, **8**(6), 6211.
- 22 J. L. Wang, L. P. Zhang, G. W. Zhao, Y. L. Gu, Z. H. Zhang, F. Zhang and W. M. Wang, *J. Solid State Chem.*, 2011, **184**, 2478.
- 23 C. Xiong and W. Tu, *Eur. J. Inorg. Chem.*, 2014, 3010.
- 24 Y. Zhu, Y. Bando, L. Yin and D. Golberg, *Chem. - Eur. J.*, 2004, **10**, 3667.
- 25 E. A. Pruss, G. L. Wood, W. J. Kroenke and R. T. Paine, *Chem. Mater.*, 2000, **12**, 19.
- 26 G. L. Wood, J. F. Janik, E. A. Pruss, D. Dreissig, W. J. Kroenke, T. Habereder, H. Noth and R. T. Paine, *Chem. Mater.*, 2006, **18**, 1434.
- 27 L. Chen, Y. Gu, L. Shi, Z. Yang, J. Ma and Y. Qian, *Solid State Commun.*, 2004, **130**, 537.
- 28 F. Liu, J. Yu, X. Ji and M. Qian, *ACS Appl. Mater. Interfaces*, 2015, **7**(3), 1824.
- 29 T. Hagio, K. Nonaka and T. Sato, *J. Mater. Sci. Lett.*, 1997, **16**, 795.
- 30 B. Zhong, X. H. Tang, X. X. Huang, L. Xia, X. D. Zhang, C. J. Wang and G. W. Wen, *Mater. Res. Bull.*, 2015, **64**, 61.
- 31 O. M. Moon, B.-C. Kang, S.-B. Lee and J.-H. Boo, *Thin Solid Films*, 2004, **464**-465, 164.
- 32 Z. F. Ying, D. Yu, H. Ling, N. Xu, Y. F. Lu, J. Sun and J. D. Wu, *Diamond Relat. Mater.*, 2007, **16**, 1579.
- 33 M. Terrones, J.-C. Charlier, A. Gloter, E. Cruz-Silva, E. Terrés, Y. B. Li, A. Vinu, Z. Zanolli, J. M. Dominguez, H. Terrones, Y. Bando and D. Golberg, *Nano Lett.*, 2008, **8**(4), 1026.
- 34 C. Tang, Y. Bando, T. Sato and K. Kurashima, *Chem. Commun.*, 2002, 1290.
- 35 A. T. Matveev, K. L. Firestein, A. E. Steinman, A. M. Kovalskii, I. V. Sukhorukova, O. I. Lebedev, D. V. Shtansky and D. Golberg, *J. Mater. Chem. A*, 2015, **3**, 20749.
- 36 A. T. Matveev, K. L. Firestein, A. E. Steinman, A. M. Kovalskii, O. I. Lebedev, D. V. Shtansky and D. Golberg, *Nano Res.*, 2015, **8**(6), 2063.